The Astrophysical Journal, 993:39 (11pp), 2025 November 1 https://doi.org/10.3847/1538-4357/ae0614

SN 2023ixf in M101: Physical Parameters from Bolometric Light Curve Modeling

József Vinkó[1,2,3,4], Zsófia Réka Bodola[2], Ákos Gődény[3], Szelina Fruzsina Csák[3], Réka Könyves-Tóth[1,2], Andrea P. Nagy[2], Tamás Szalai[2], Dominik Bánhidi[5], Imre Barna Bíró[5,6], Attila Bódi[1,7], Zsófia Bora[1,3], István Csányi[5], Borbála Cseh[1,8], Tibor Hegedüs[5], Ágoston Horti-Dávid[1,3], András Péter Joó[1,3], Csilla Kalup[1,3], Levente Kriskovics[1], Erika Mochnács[2], András Pál[1], Zsolt Regály[1], Bálint Seli[1,3], Ádám Sódor[1], Norton Olivér Szabó[1,3], Róbert Szakáts[1], Péter Székely[2,9], Vázsony Varga[1,3], and Krisztián Vida[1]
[1] HUN-REN CSFK Konkoly Observatory, MTA Centre of Excellence, Konkoly Thege M. út 15-17, Budapest, 1121, Hungary; vinko.jozsef@csfk.hun-ren.hu
[2] Department of Experimental Physics, Institute of Physics, University of Szeged, Dóm tér 9, Szeged, 6720, Hungary
[3] ELTE Eötvös Loránd University, Institute of Physics and Astronomy, Pázmány Péter sétány 1A, Budapest 1117, Hungary
[4] Department of Astronomy, University of Texas at Austin, 2515 Speedway, Stop C1400, Austin, TX 78712-1205, USA
[5] Baja Observatory of University of Szeged, Szegedi út, Kt. 766, Baja, 6500, Hungary
[6] HUN-REN-SZTE Stellar Astrophysics Research Group, Szegedi út, Kt. 766, Baja, 6500, Hungary
[7] Department of Astrophysical Sciences, Princeton University Peyton Hall, 4 Ivy Lane, Princeton, NJ 08544, USA
[8] MTA-ELTE Lendület "Momentum" Milky Way Research Group, Hungary
[9] Semilab Inc., Prielle Kornélia utca 2, Budapest, 1117, Hungary
Received 2024 September 6; revised 2025 September 1; accepted 2025 September 2; published 2025 October 23

Abstract

We present new photometric observations of the core-collapse supernova SN 2023ixf occurred in M101, taken with the RC 80 and BRC80 robotic telescopes in Hungary. The initial nickel mass from the late-phase bolometric light curve extending up to 400 days after explosion, is inferred as $M_{\rm Ni} = 0.046 \pm 0.007\ M_\odot$. The comparison of the bolometric light curve with models from hydrodynamical simulations as well as semi-analytic radiative diffusion codes reveals a relatively low-mass ejecta of $M_{\rm ej} \lesssim 9\ M_\odot$, contrary to SN 2017eaw, another H-rich core-collapse event, which had $M_{\rm ej} \gtrsim 15\ M_\odot$.

Unified Astronomy Thesaurus concepts: Type II supernovae (1731); Core-collapse supernovae (304); Radiative processes (2055); Late stellar evolution (911)

Materials only available in the online version of record: data behind figure

1. Introduction

The discovery of SN 2023ixf (K. Itagaki 2023) at very early phase ($\lesssim$1 day after first light; D. Hiramatsu et al. 2023) in the nearby galaxy M101 ($D_{\rm L} \simeq 6.85$ Mpc; A. G. Riess et al. 2022) triggered a particularly intense study of its progenitor as well as the early-phase interaction between a H-rich ejecta of a core-collapse supernova with the confined circumstellar matter (CSM) envelope in the immediate vicinity of the exploding star. From preexplosion space- and ground-based photometry, a red supergiant progenitor star ($\log(L/L_\odot) \sim 5$, $T_{\rm eff} \simeq$ 3500–4000 K, $\log(R/R_\odot) \sim 2.7$) was identified, which was enshrouded by a thick, dusty CSM (J. E. Jencson et al. 2023; C. D. Kilpatrick et al. 2023; Z. Niu et al. 2023; J. L. Pledger & M. M. Shara 2023; Y.-J. Qin et al. 2024; M. Soraisam et al. 2023; G. Li et al. 2024, 2025; J. M. M. Neustadt et al. 2024; C. L. Ransome et al. 2024; S. D. Van Dyk et al. 2024; D. Xiang et al. 2024; D. Dickinson et al. 2025; W. V. Jacobson-Galán 2025; M. Shrestha et al. 2025; W. Zheng et al. 2025). Interestingly, the initial mass ($M_{\rm ZAMS}$) of the progenitor turned out to be quite uncertain. It was estimated to be in a wide range of masses, from 9 to 20 $M_\odot$, and having a bimodal distribution: about half of the studies reported a relatively low $M_{\rm ZAMS}$ (11–14 $M_\odot$), while others found it in between 16 and 22 $M_\odot$ (see Table 1 in W. V. Jacobson-Galán 2025). The more massive progenitor ($M_{\rm prog} \sim 22\ M_\odot$, implying an even higher $M_{\rm ZAMS}$) was also favored by C. Liu et al. (2023) using IFU spectroscopy and population synthesis of the surroundings of the SN site. This notable uncertainty in the progenitor mass is probably related to the presence of the thick, compact CSM that may have significantly affected the preexplosion photometric data.

Later, along with the accumulation of photometric/spectroscopic data of the SN itself, the estimation of the progenitor mass became possible via modeling the light curve (LC). As emphasized by M. C. Bersten et al. (2024), LC modeling could be a powerful tool that may be able to provide additional constraints on the physical parameters of the progenitor that are less affected by the uncertainties of the direct, preexplosion measurements of the usually very faint progenitor.

Most of the results from LC modeling published so far favored the low-mass progenitor. D. Hiramatsu et al. (2023) found $M_{\rm prog} \sim 11\ M_\odot$ implying $M_{\rm ZAMS} \sim 12\ M_\odot$, similar to the results of M. C. Bersten et al. (2024; $\sim$12 $M_\odot$), A. Singh et al. (2024; $\sim$10 $M_\odot$), A. Kozyreva et al. (2025; $\sim$10 $M_\odot$), Q. Fang et al. (2025; $\lesssim$9.5 $M_\odot$), and S. P. Cosentino et al. (2025; $\sim$9 $M_\odot$). These studies compared the synthesized LCs of pre-existing (e.g., T. J. Moriya & A. Singh 2024) or newly computed (M. C. Bersten et al. 2024) hydrodynamical simulations with the observations, in order to constrain the ejecta (and the progenitor, via stellar-evolution models) mass. The relatively low-mass progenitor is consistent with the results of E. A. Zimmerman et al. (2024), who used the integrated bolometric luminosity of the SN to estimate the ejecta mass as $M_{\rm ej} \sim 7.5\ M_\odot$, implying $M_{\rm ZAMS} \lesssim 10\ M_\odot$.

Some other studies, however, found somewhat higher progenitor masses. For example, Y.-P. Yang et al. (2024)

applied semianalytic scaling relations to their griz photometric data, and inferred a somewhat broader range for the possible ejecta mass, $M_{\rm ej} \sim 4$–$16\ M_\odot$.

On the other hand, based on new MESA+STELLA model computations, B. Hsu et al. (2025) pointed out that the relatively low ejecta mass, $M_{\rm ej} \lesssim 8\ M_\odot$, does not necessarily imply low ZAMS mass for the progenitor. Their best-fit models had initially $M_{\rm ZAMS} \sim 17.5$–$21.5\ M_\odot$, but all of them lost almost half of their initial mass, and ended up having only $M_{\rm prog} = 7$–$8\ M_\odot$ at the moment of core collapse. They also proposed that it may be possible to break the degeneracy between the physical parameters inferred from photometry by detecting and measuring the pulsational variability of the progenitor prior to core collapse. Similarly, S. Forde & J. A. Goldberg (2025) found that MESA+STELLA models having $M_{\rm prog} \sim 15\ M_\odot$ and $M_{\rm ZAMS} \sim 23\ M_\odot$ (implying significant mass loss) describe the LC at the end of the plateau phase better than lower mass progenitor models with less amount of mass loss.

After SN 2023ixf entered into the nebular phase, L. Ferrari et al. (2024) presented a new constraint on the initial mass of the progenitor based on nebular spectroscopy. From the line ratios of forbidden [O I] and [Ca II] emission features, they inferred $12 < M_{\rm ZAMS} < 15\,M_\odot$ for the initial mass of the progenitor. Note, however, that $12\,M_\odot$ was the lowest initial mass they considered, and the actual ejecta mass probed by the nebular spectra depends on the mass-loss history of the progenitor, which is uncertain. Since then many similar results were published, all within the range of $M_{\rm ZAMS} \sim 15 \pm 5\ M_\odot$, by independent groups (Q. Fang et al. 2025; G. Folatelli et al. 2025; A. Kumar et al. 2025; G. Li et al. 2025; P. D. Michel et al. 2025; W. Zheng et al. 2025).

The apparent diversity in the published ZAMS/progenitor masses of SN 2023ixf suggests that this issue is still far from being resolved. In this paper we present an independent LC modeling of SN 2023ixf by applying two different approaches: we use the semianalytic code LC2[10] (A. P. Nagy et al. 2014; A. P. Nagy & J. Vinkó 2016) and the hydrodynamical code SNEC[11] (V. Morozova et al. 2015) for synthesizing Type II SN LCs and comparing them with the bolometric data assembled from the observations. We also use SN 2017eaw, another H-rich Type II-P event, as a comparison object to highlight the similarities and differences between the physical parameters of the two SNe.

2. Observations

For SN 2023ixf, optical photometric data were collected through *BV griz* filters with the two 0.8 m robotic telescopes (RC 80 and BRC80) operating at Piszkéstető station of Konkoly Observatory and at Baja Observatory of University of Szeged, Hungary. For the description of the telescopes, as well as details on the data reduction and photometry, see B. Barna et al. (2023). The *BV griz* light curve is shown in Figure 1. It illustrates the previous finding that SN 2023ixf was a "hybrid" Type IIP/IIL event characterized by a shorter plateau and higher LC decline rate during the plateau phase (e.g., A. Singh et al. 2024).

From the multiband photometric data the spectral energy distribution was assembled for each epoch, and it was integrated over wavelength to get a pseudo-bolometric LC in a similar way as in T. Szalai et al. (2019). For the ultraviolet (UV) fluxes we used Swift photometry collected from E. A. Zimmerman et al. (2024). The UV fluxes had significant contribution on the integrated bolometric LC only during the first ∼30 days after explosion. For the infrared (IR) part, a Rayleigh–Jeans tail was fitted to the z-band fluxes, and it was integrated between λ_z and infinity to estimate the (unobserved) IR contribution at each epoch.

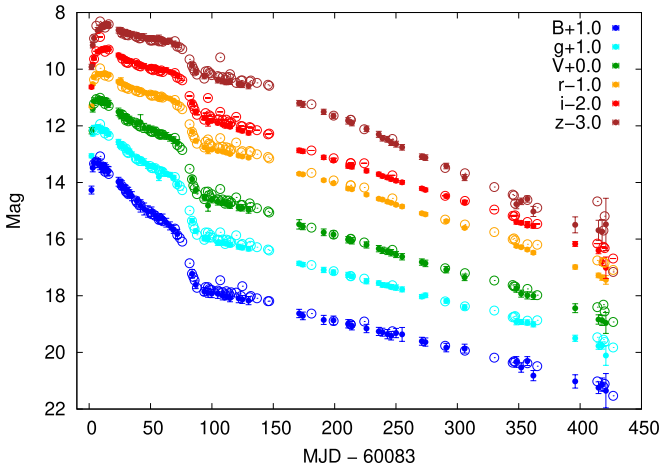

Figure 1. *BVgriz* light curve of SN 2023ixf. Data from Konkoly and Baja are plotted with filled and open symbols, respectively. Different filters are color-coded, and a small vertical offset was applied between them for display purposes, as indicated in the legend.

(The data used to create this figure are available in the online article.)

For the total (Milky Way and M101) interstellar extinction we applied $E(B–V) = 0.035$ mag from C. Liu et al. (2023), which is based on high-resolution spectra of SN 2023ixf, and assumed standard reddening law with $R_V = 3.1$.

Finally, we adopted the luminosity distance of M101 from A. G. Riess et al. (2022; $D_L \simeq 6.85$ Mpc), which is based on the most recent calibration of Cepheids, to get the luminosity as a function of time. The uncertainty of the distance is estimated by S. D. Van Dyk et al. (2024) as ±0.32 Mpc.

The final pseudo-bolometric LC is plotted in Figure 2, together with that of SN 2017eaw taken from T. Szalai et al. (2019). Our pseudo-bolometric LC for SN 2023ixf looks similar to that of E. A. Zimmerman et al. (2024), but it lacks the first, very high luminosity peak at $t \lesssim 4$ days after explosion that was published by L. Martinez et al. (2024; but see A. Kozyreva et al. 2025 for the ambiguity of the "observed" bolometric LC). Since we do not aim to model the early-ejecta–CSM interaction, the uncertainty of the bolometric LC during the first few days does not prevent the analysis of the rest of the LC.

From Figure 2 it is immediately seen that while the luminosity evolution of SN 2017eaw closely follows the expected decline due to the radioactive decay of ^{56}Co (at least up to ∼450 days), it is not the case for SN 2023ixf. Such a faster luminosity decline is usually a consequence of a lower ejecta mass, when the SN envelope becomes progressively transparent to gamma rays released by radioactive processes more quickly than in the case of a more massive ejecta. The physical parameters of these two SNe are modeled and compared in the following sections.

[10] http://titan.physx.u-szeged.hu/~nagyandi/LC2.2/
[11] https://stellarcollapse.org/index.php/SNEC.html

3. Modeling

This section contains the details of the semianalytical and hydrodynamical models we built for SN 2023ixf. The results are presented in Section 4.

3.1. Nickel Mass

For measuring the initial nickel mass, we fit the bolometric luminosity during the tail phase (i.e., after the end of the plateau at $t > 100$ days) with

$$L(t) = \frac{M_{\rm Ni}}{M_\odot} \times \left(L_\gamma(t) \times \left(1 - \exp\left[-\frac{T_\gamma}{t} \right] \right) + L_+(t) \right), \quad (1)$$

where

$$L_\gamma(t) = C_1 \times e^{-t/8.8} + 0.968 \cdot C_2 \times e^{-t/111.3}, \quad (2)$$

represents the energy input from the deposition of γ-rays produced by the Ni-Co radioactive decay, with t being in days, $C_1 = 6.45 \times 10^{43}$ erg s^{-1} and $C_2 = 1.45 \times 10^{43}$ erg s^{-1}, while

$$L_+(t) = 0.032 \cdot C_2 \times (e^{-t/111.3} - e^{-t/8.8}) \quad (3)$$

describes the contribution from the thermalization of the kinetic energy of positrons produced by the Co-decay (e.g., S. Valenti et al. 2008; D. Branch & J. C. Wheeler 2017). Our model has a very minor difference from that used by B. Hsu et al. (2025), since we treat the contribution from positron trapping separately from the γ-rays.

The γ-ray deposition is parametrized by the exponent T_γ, which is connected with the ejecta mass and kinetic energy as

$$T_\gamma = M_{\rm ej} \sqrt{\frac{9}{40\pi} \frac{\kappa_\gamma}{E_{\rm kin}}} \quad (4)$$

for a constant density ejecta (D. Branch & J. C. Wheeler 2017). For the gamma-ray opacity we adopted $\kappa_\gamma = 0.028$ cm^2 g^{-1} (S. A. Colgate et al. 1980).

By fitting Equation (1) to the bolometric light curve of SN 2023ixf after $t > 100$ days we get $M_{\rm Ni} = 0.046 \pm 0.007\ M_\odot$ and $T_\gamma = 238 \pm 6$ days. The latter corresponds to a mass of $M_{\rm ej} = 7.3 \pm 0.2\ M_\odot$ for a constant density ejecta and $E_{\rm kin} \sim 10^{51}$ erg via Equation (4). For comparison, a similar analysis with the bolometric data of SN 2017eaw results in $M_{\rm Ni} = 0.054 \pm 0.006\ M_\odot$, $T_\gamma \sim 557$ days and $M_{\rm ej} \sim 17.0\ M_\odot$ (note that the formal errors for T_γ are too high in this case, as the bolometric decline rate of SN 2017eaw is very close to the Co-decay rate that would correspond to $T_\gamma \to \infty$).

Our inferred nickel mass is consistent with the results of P. D. Michel et al. (2025; $M_{\rm Ni} = 0.049\ M_\odot$), M. C. Bersten et al. (2024; 0.05 $M_\odot$), G. Li et al. (2025; 0.059 $M_\odot$), A. Singh et al. (2024; 0.06 $M_\odot$), and T. J. Moriya & A. Singh (2024; ~0.04–0.06 $M_\odot$). Other studies found slightly higher nickel masses, e.g., $M_{\rm Ni} = 0.07\ M_\odot$ (B. Hsu et al. 2025; E. A. Zimmerman et al. 2024; S. P. Cosentino et al. 2025) up to $M_{\rm Ni} = 0.098\ M_\odot$ (Y.-P. Yang et al. 2024). Note that beside the photometric errors, the nickel mass estimates are directly influenced by the systematic uncertainty of the assumed distance. In this paper we adopted $D_L = 6.85 \pm 0.35$ Mpc (see Section 2), thus, the relative error of the distance is $\delta D_L = 0.05$. This corresponds to a systematic uncertainty of the initial nickel mass of $\pm 0.002\ M_\odot$, which is much lower than the scattering of the various nickel mass estimates appeared in the literature. Thus, it is probable that the source of the disagreement is mostly the uncertainties of the bolometric light curves used in different studies.

From this approximate analysis of the late-phase LC we conclude that, in accord with Figure 2, the faster luminosity decline of SN 2023ixf compared to that of SN 2017eaw can be explained by a factor of ~2 lower ejecta mass of SN 2023ixf, if the kinetic energy of the two events were similar to the canonical $E_{\rm kin} \sim 10^{51}$ erg.

A more detailed modeling of the whole bolometric LC is presented below.

Table 1
Parameters of the Semianalytic LC2 Models

Parameter	SN 2023ixf		SN 2017eaw	
	Shell	Core	Shell	Core
Initial radius (10^{13} cm)	20	1.5	4.7	3.3
Ejecta mass ($M_\odot$)	0.35	7.5	0.39	14.0
Nickel mass ($M_\odot$)	0	0.046	0	0.043
Kinetic energy (10^{51} erg)	0.04	1.25	0.11	1.80
Thermal energy (10^{51} erg)	0.025	1.00	0.07	0.90
Recombination temperature (K)	0	7500	0	7500
Mean opacity (cm^2 g^{-1})	0.34	0.2	0.34	0.2
Magnetar energy (10^{51} erg)	0	0	0	0.002
Magnetar spin down (day)	0	0	0	100

3.2. Complete LC Modeling

We utilized two different codes to model the entire bolometric light curve of SN 2023ixf, except the earliest high-luminosity peak caused by ejecta–CSM interaction. First, we used LC2 (A. P. Nagy et al. 2014; A. P. Nagy & J. Vinkó 2016), which is a semianalytic code based on the radiation-diffusion model of W. D. Arnett (1980, 1982) and W. D. Arnett & A. Fu (1989), including H-recombination. The latest version (LC2.2) was adopted, which, in addition to the radioactive decay of ^{56}Ni–^{56}Co and H-recombination, contains an optional energy input from the spin down of a magnetized neutron star (D. Kasen & L. Bildsten 2010). We used the two-component "core+shell" model, where the "shell" component describes the first part ($\lesssim$30 days) of the LC, while the "core" component models the rest of that. Since our model does not contain the energy released by the ejecta–CSM interaction that may significantly affect the early part of the LC, the "shell" parameters may not be physically self-consistent with those of the "core" component.

Table 1 lists the input parameters of LC2 as well as their best-fit values[12] for SN 2023ixf and SN 2017eaw. The recombination temperature and the mean optical opacity for the core component were fixed at 7500 K and 0.2 cm^2 g^{-1}, respectively (see A. P. Nagy & J. Vinkó 2016). Since the low-mass shell component was assumed to be H-rich, its opacity was fixed at $\kappa = 0.34$ cm^2 g^{-1}, and H-recombination was ignored in the shell.

Following the plateau phase, when the H-rich envelope recombines and becomes mostly transparent, the luminosity evolution is expected to follow the energy input due to the radioactive decay of ^{56}Co. During this radioactive tail phase

[12] All models were computed manually, without applying any automated fitting routine, due to the strong parameter degeneracy. Thus, the reported best-fit values represent only a possible solution for the strongly ill-constrained problem.

the observed luminosity decline is governed by the trapping of gamma rays and positrons released by the Co-decay. For the gamma-ray opacity we adopted $\kappa_\gamma = 0.028$ cm^2 g^{-1} (S. A. Colgate et al. 1980), while for positrons we applied an effective opacity of $\kappa_+ = 7.0$ cm^2 g^{-1} (S. Valenti et al. 2008).

Second, we applied the 1D Lagrangean hydrocode SNEC version 1.00 (V. Morozova et al. 2015) to synthesize bolometric light curves from the simulated explosion of certain model stars. For the input models we used MESA version r-12778 (B. Paxton et al. 2011, 2013, 2015, 2018, 2019; A. S. Jermyn et al. 2023) to construct models of $M_{\rm ZAMS} = 11$, 12, 15, 20 and 25 $M_\odot$ stars, and let them evolve until core collapse.

We ran the 11 $M_\odot$ model (M11 hereafter), following the `example_make_pre_ccsn` test suite, with $Z = 0.006$ initial metallicity and used the "Dutch" hot-wind scheme with $\eta = 0.8$ scaling factor (T. Nugis & H. J. G. L. M. Lamers 2000; E. Glebbeek et al. 2009). For convection we considered overshooting by setting the diffusion mixing coefficient as $f_0 = 0.004$ and $f = 0.01$, and used the Ledoux criterion with 0.01 α semiconvection. For the 20 $M_\odot$ model (M20 hereafter) we followed the `25M_pre_ms_core_collapse` test suite considering $Z = 0.02$ initial metallicity and adopting the same wind scheme and convection as for the 11 $M_\odot$ model. In order to cover the parameter space for the LC fitting, we built further models with the same prescription as for M20. We created models with 12 $M_\odot$ (M12 hereafter), 15 $M_\odot$ (M15n hereafter) and 25 $M_\odot$ (M25 hereafter). Unlike the M11 model, M12 did not run into numerical difficulties when solar metallicity was assumed, thus, M12 was also built assuming $Z = 0.02$. Note that the SNEC source code also contains a $M_{\rm ZAMS} = 15$ $M_\odot$ model (M15o hereafter) that was built with an earlier version of MESA. Since the main parameters of that model (progenitor mass and radius, density distribution, etc.) are different from those of our M15n model, we used M15o model as an input in SNEC as well.

In order to test the effect of the confined CSM on the LC, we attached an extended envelope on top of the MESA models using the two-component CSM model given by N. Kuriyama & T. Shigeyama (2020), D. Tsuna et al. (2021), and D. Tsuna & Y. Takei (2023), which assumes a single eruption from the progenitor years before the explosion. We followed the interpretation of D. Tsuna & Y. Takei (2023) to construct the CSM as

$$\frac{\rho_{\rm CSM}(r)}{\rho_0} = \left[\frac{1}{2}\left(\left(\frac{r}{r_{\rm CSM}}\right)^{\frac{1.5}{y}} + \left(\frac{r}{r_{\rm CSM}}\right)^{\frac{n_{\rm out}}{y}}\right)\right]^{-y} \quad (5)$$

where $\rho_0 \approx M_{\rm CSM}/(37 \cdot r_{\rm CSM}^3)$, see Equation (2) and Equation (3) and their detailed description in D. Tsuna & Y. Takei (2023). Based on D. Tsuna et al. (2021) we applied the parameters of an RSG progenitor, $y = 2$ and $n_{\rm out} = 12$. This way we created a CSM model with a double power-law density profile, dividing the CSM to a bound and an unbound part, and attached it to the outmost part of the stellar envelope with no gap in between them. The key parameters of the CSM (total mass and outer radius) were set similar to the literature results cited above and also the mass and the radius of the "shell" component of the LC2 model.

In SNEC we adopted the "Thermal Bomb" explosion model and the input physical parameters listed in Table 2. The opacity floor of $\kappa_{\rm min}^{\rm core} = 0.24$ and $\kappa_{\rm min}^{\rm env} = 0.01$ cm^2 g^{-1} was adopted for the core and the envelope, respectively. The mass of the neutron star remnant ($M_{\rm NS}$) was assumed to be equal to the excised mass, an input parameter in SNEC. In some models it was set as 1.4 $M_\odot$ (the default value in SNEC), but for most of them it was defined to be equal to the mass of the iron core of the input MESA model.

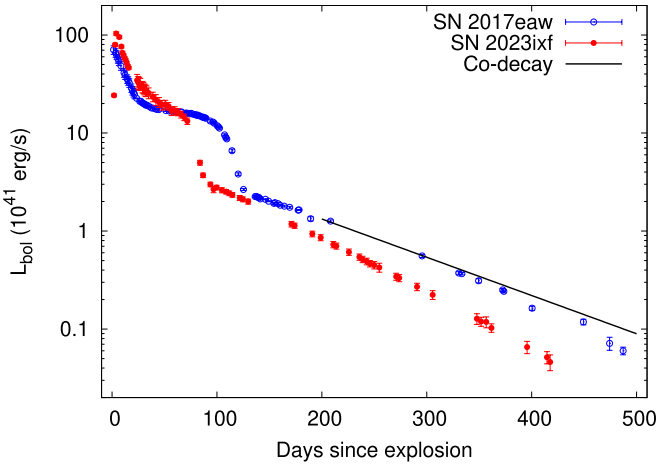

Figure 2. The pseudo-bolometric light curves of SN 2023ixf (red) and SN 2017eaw (blue). The black line represents the expected luminosity decline due to the radioactive decay rate of ^{56}Co.

The model parameters applied in the SNEC simulations are summarized in Table 2. The ejecta masses are calculated as $M_{\rm ej} = M_{\rm prog} - M_{\rm NS}$. Since SNEC does not compute explosive nucleosynthesis, the initial mass of radioactive ^{56}Ni is another input parameter. For that we adopted the nickel mass derived in Section 3.1, except for M20-3-csm and M25-csm, where $M_{\rm Ni} = 0.03$ $M_\odot$ was used in order to better match the early tail luminosity of the $M \gtrsim 20$ $M_\odot$ models. In each model (except M15o-ni, see later) the distribution of ^{56}Ni was assumed to extend up to 3 $M_\odot$ within the ejecta in mass coordinates. The corresponding maximum velocity ($v_{\rm Ni}^{\rm max}$) is given in Table 2 to indicate the degree of mixing in the ejecta. The $E_{\rm tot}$ energy is the actual energy released by the thermal bomb, while $E_{\rm final}$ (also an input parameter) represents practically the asymptotic kinetic energy at late phases (V. Morozova & J. M. Stone 2018).

The last column of Table 2 indicates whether the boxcar smoothing algorithm were applied during the simulation: 1 means yes, 0 means no. Smoothing mimics the effect of mixing during the explosion, thus, it is generally applied in SNEC simulations (V. Morozova & J. M. Stone 2018). The reason for switching it off in some models was the finding that it also makes the end of the plateau shallower and somewhat shorter, which is not consistent with the observed LC of SN 2023ixf (see also S. Forde & J. A. Goldberg 2025).

4. Results and Discussion

In this section we present and discuss the results from the two modeling approaches (semianalytic versus hydrodynamical) and their implications to the progenitor of SN 2023ixf.

4.1. LC2 Models

The output luminosities of the LC2 models that were found to best represent the observations are plotted in Figures 3 and 4 for SNe 2023ixf and 2017eaw, respectively. In these plots the

Table 2
Parameters of the SNEC Models for SN 2023ixf

Model	$M_{\rm ini}$ ($M_\odot$)	$M_{\rm prog}$ ($M_\odot$)	$R_{\rm prog}$ (10^{13} cm)	$M_{\rm csm}$ ($M_\odot$)	$R_{\rm csm}$ (10^{13} cm)	$M_{\rm Ni}$ ($M_\odot$)	$M_{\rm NS}$ ($M_\odot$)	$M_{\rm ej}$ ($M_\odot$)	$E_{\rm tot}$ (foe)	$E_{\rm final}$ (foe)	$v_{\rm Ni}^{\rm max}$ (km s^{-1})	sm
M11	11	10.26	3.04	⋯	⋯	0.046	1.40	8.86	2.23	1.20	1277	0
M11-csm1	11	10.26	3.04	0.35	20.0	0.046	1.40	8.86	2.26	1.60	1448	0
M11-csm2	11	10.26	3.04	0.35	60.0	0.046	1.59	8.67	1.97	1.60	1392	1
M11-csm3	11	10.26	3.04	0.35	25.0	0.046	1.59	8.67	1.97	1.60	1392	1
M11-csm4	11	10.26	3.04	0.18	20.0	0.046	1.59	8.67	1.98	1.60	1393	1
M11-csm5	11	10.26	3.04	0.50	30.0	0.046	1.59	8.67	1.98	1.60	1399	1
M12	12	10.42	5.03	⋯	⋯	0.046	1.50	8.92	3.08	1.60	1985	1
M12-csm	12	10.42	5.03	0.35	20.0	0.046	1.50	8.92	3.08	1.60	1977	1
M12-2-csm	12	10.42	5.03	0.35	20.0	0.046	1.60	8.82	2.37	1.20	1737	0
M15o	15	12.29	7.23	⋯	⋯	0.046	1.40	10.89	1.84	1.20	1353	1
M15o-csm1	15	12.29	7.23	0.35	20.0	0.046	1.40	10.89	1.89	1.25	1384	1
M15o-csm2	15	12.29	7.23	0.35	60.0	0.046	1.60	10.69	1.58	1.20	1303	1
M15o-ni	15	12.29	7.23	0.35	20.0	0.046	1.40	10.89	1.89	1.25	5268	1
M15n	15	11.69	6.60	⋯	⋯	0.046	1.50	10.19	2.18	1.20	1671	1
M15n-csm	15	11.69	6.60	0.35	20	0.046	1.50	10.19	2.18	1.20	1853	1
M15n0-csm	15	11.69	6.60	0.35	20	0.046	1.50	10.19	1.99	1.00	1695	0
M15n1-csm	15	11.69	6.60	0.35	20	0.046	1.40	10.29	2.58	1.00	1639	0
M15n2-csm	15	11.69	6.60	0.35	20	0.046	1.50	10.19	2.19	1.20	1876	0
M20	20	15.85	6.83	⋯	⋯	0.046	1.40	14.45	4.30	1.80	1672	1
M20-csm	20	15.85	6.83	0.35	20.0	0.046	1.40	14.45	4.30	1.80	1699	0
M20-2-csm	20	15.85	6.83	0.35	20.0	0.046	1.76	14.09	2.73	1.20	1305	0
M20-3-csm	20	15.85	6.83	0.35	20.0	0.030	1.76	14.09	3.03	1.50	1527	0
M20-csm2	20	15.85	6.83	0.35	60.0	0.046	1.76	14.09	3.32	1.80	1672	1
M25	25	20.75	5.78	⋯	⋯	0.046	1.99	18.76	3.05	1.80	1391	0
M25-csm	25	20.75	5.78	0.35	20.0	0.030	1.99	18.76	3.05	1.80	1363	0

Note. The last column indicates whether `boxcar_smoothing` was applied (1) or not (0) in the model.

top panel contains the whole observed light curve, while the bottom panel shows only the first 150 days, and the "core" and "shell" components alone are plotted as well. The "shell" component contributes only during the first 30–40 days.

As seen in Figures 3 and 4, both the level and the length of the LC plateau are modeled very well by the LC2 code for both SN 2023ixf and SN 2017eaw. The same is true for the radioactive tail part, when the light curve decline rate is affected by the ^{56}Co-decay as well as the gamma-ray leaking due to the dilution of the expanding ejecta. The key parameter for these two effects are the initial nickel mass ($M_{\rm Ni}$) and the ejecta mass ($M_{\rm ej}$) together with the kinetic energy ($E_{\rm kin}$) as detailed in Section 3.1. It is important to note that the latter two parameters also affect the LC during the plateau phase: higher $M_{\rm ej}$ makes the plateau longer, while higher $E_{\rm kin}$ shortens it (e.g., A. P. Nagy et al. 2014). The fact that the LC2 model fits both the plateau and the tail simultaneously with the same set of parameters makes strong constraints on them, especially on the ejecta mass that we focus on.

The constraint on the ejecta mass is also strengthened by the fit to the LC of SN 2017eaw. In that case both the plateau is longer and the decline during the tail is shallower, which is explained self-consistently by the larger $M_{\rm ej}$ (see Table 1). Note that the fitting of the late-phase decline needed a small amount of magnetar input in addition to the radioactive decay energy. Nevertheless, it is seen that SN 2017eaw very likely had a factor of ∼2 higher ejecta mass than SN 2013ixf, which is consistent with the previous estimate in Section 3.1.

It might be interesting that the initial radii of the outer "shell" components differ by almost an order of magnitude for the two SNe. For SN 2023ixf, the $R_0 \sim 2 \times 10^{14}$ cm value looks similar to the radius of the dense confined CSM (S. D. Van Dyk et al. 2024; E. A. Zimmerman et al. 2024), even though it might be only a coincidence as the LC2 model assumes a constant density profile for the shell, while the density of confined CSM usually decreases outward. Nevertheless, the shell radius for SN 2017eaw turned out to be much smaller, which is consistent with the moderate early CSM interaction in that case.

4.2. SNEC Models

Figure 5 presents the evolution of the luminosities (top panels) and the photospheric velocities (bottom panels) for the M11/M12, M15, M20, and M25 SNEC models, respectively, together with the observations for SN 2023ixf. For the luminosities we used the pseudo-bolometric LC derived in Section 2, while for the velocities we adopted the fit to the observed velocities from A. Singh et al. (2024) as $v_{\rm obs} \simeq 4350 \cdot (t_d/53)^{-0.47}$, where t_d is the time since explosion in days, for $t_d > 20$ days.

It is known that the observed velocities, usually calculated from the Doppler-shift of the absorption minimum of certain features, like Fe II λ5169 or $H\beta$, usually overestimate the photospheric velocities inferred directly from hydrodynamical models assuming $\tau_{\rm ph} = 1$ or $2/3$ as the optical depth of the photosphere (e.g., J. A. Goldberg et al. 2019; B. L. Barker et al. 2022). In order to take this effect into account, the observed velocities were corrected as $v_{\rm phot} \approx v_{\rm obs} - 600$ km s^{-1} before plotting in Figure 5.

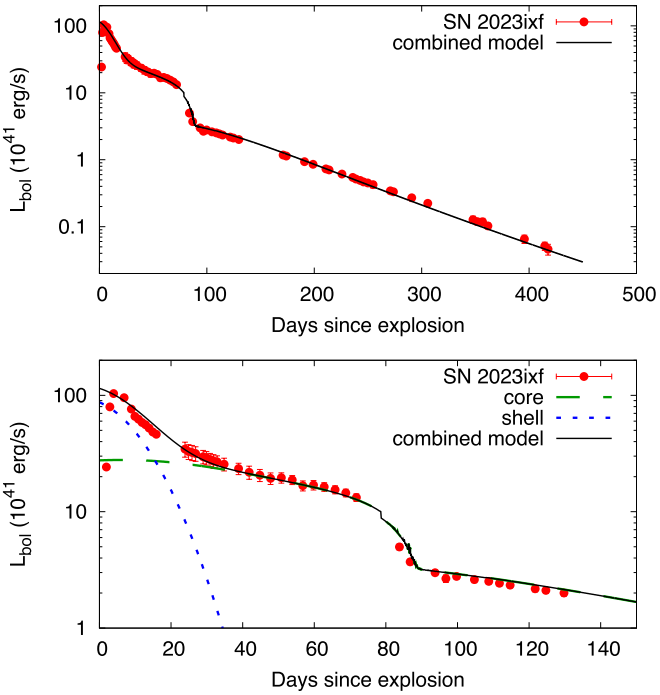

Figure 3. The bolometric LC of SN 2023ixf plotted together with the semianalytic LC2 model shown in Table 1. The top panel shows the data with the combined (core+shell) model, while the bottom panel displays the core and shell components separately, as well. See text for explanation.

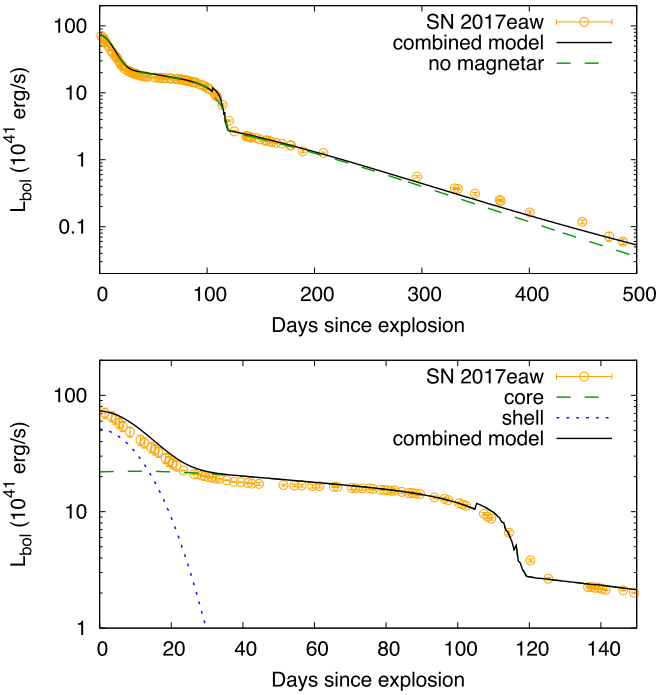

Figure 4. The same as Figure 3 but for SN 2017eaw. The dashed line in the upper panel represents the model without the energy input from the magnetar.

It is seen that all models containing the extended CSM have the luminosity peak at least an order of magnitude brighter than the observations (see also A. Kozyreva et al. 2025). Thus, in the followings we consider only the $t > 30$ days phases when comparing the model LCs with the data (S. Forde & J. A. Goldberg 2025). We do not attempt to optimize the parameters of the CSM to fit the early-phase data, because (i) this topic has been already explored extensively in the literature, and (ii) SNEC may not be the best modeling code to predict the luminosity of the shock wave propagating in such environments, where, for example, the deviation from LTE may be substantial. Even though we focus on modeling the LC after shock breakout from the confined CSM, we explore the effect of varying the CSM parameters on the behavior of the late-phase LC in the next subsection.

Figure 5 shows that the M15o, M20 and M25 models, both with and without the CSM envelope, overpredict the luminosity for the plateau phase after $t \gtrsim 30$ days. The M15n models are closer to the observed plateau luminosity, but they start the transition to the tail phase about ∼10 days earlier than observed.

Moreover, these high-mass models, all having $M_{ej} > 10\ M_{\odot}$, are also not consistent with the luminosity during the early tail phase: for $t > 80$ days all of them, except M15n1-csm, M20-3-csm, and M25-csm, predict slightly higher luminosities than observed. At first this may be surprising, because all these models, except M20-3-csm and M25-csm, were computed with the same amount of M_{Ni} (0.046 $M_{\odot}$) that represents the best-fit to the observed tail light curve presented in Section 3.1. The probable reason for this discrepancy is that in these models the luminosity at the beginning of the tail phase (between $100 < t < 120$ days) has not yet settled to the level of the radioactive decay. Thus, the model LC shortly after the end of the plateau may still contain some energy input from the remaining photosphere. This means that the model LC at these early tail phases may underestimate the Ni-masses when compared to the observations. This is illustrated by the models M20-3-csm and M25-csm that produce better fits to the data at the early tail phases: these models were computed assuming $M_{Ni} = 0.03\ M_{\odot}$, instead of 0.046 $M_{\odot}$ used in all the other models.

The M15n1-csm model is unique in a sense that it fits the early tail luminosity even though it was computed with $M_{Ni} = 0.046\ M_{\odot}$; thus, it seems to contradict with the above statement. However, in this model the excised mass (practically the mass of the remnant neutron star) was set at 1.4 $M_{\odot}$, instead of 1.5 $M_{\odot}$, the latter being the mass of the iron core in the M15n model family. The output of this model illustrates some model-dependency of the tail luminosity predicted by SNEC: it is sensitive to the value of the parameter `mass_excised`. Exploring this effect more thoroughly is, however, beyond the scope of this paper.

The LCs from the M11 and M12 model families (having $M_{ej} < 9\ M_{\odot}$) are the most similar to the observed bolometric LC at the late-plateau phase, after ∼30 days, as well as during the radioactive tail phase (Figure 5; top-left panel). The M11-csm model looks like the optimal one, because it fits both the mid-plateau luminosity as well as the length of the plateau adequately.

Regarding the velocities shown in Figure 5, all of the SNEC models considered here are more-or-less consistent with the observed velocities, at least for $t < 60$ days, if one takes into account the well-known offset between the observed and the model velocities (∼600 km s^{-1}; see above). This is consistent with the result of J. A. Goldberg et al. (2019) who found that "ejecta velocities measured during the majority of the plateau phase provide little additional information about explosion characteristics." On the other hand, in principle, models that predict velocities that are clearly incompatible with the observed ones can be ruled out (see, e.g., V. P. Utrobin &

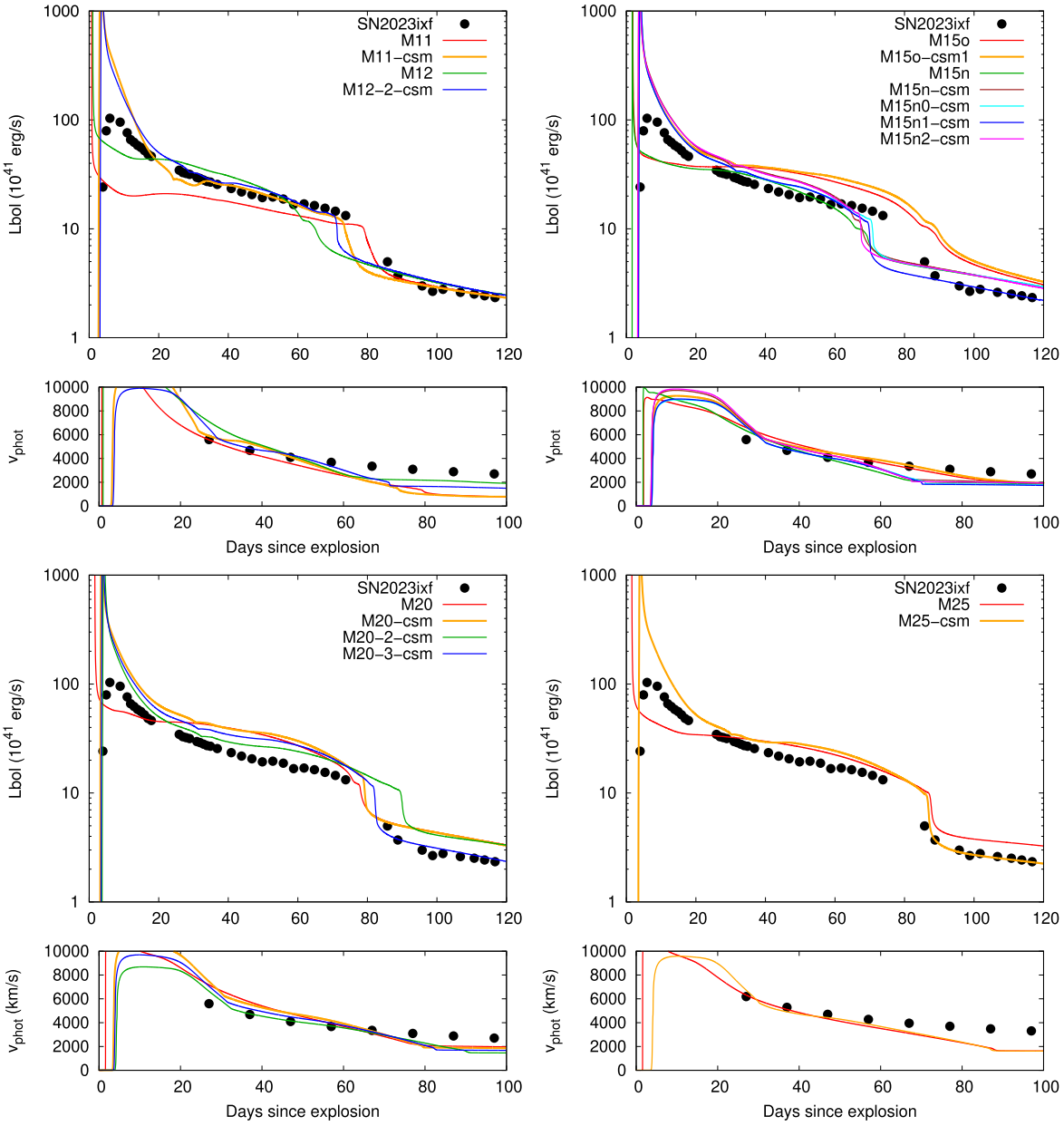

Figure 5. SNEC model luminosities and photospheric velocities (colored curves) plotted together with the observed data (black circles). The observed velocities, derived from the Fe II λ5189 feature, were decreased by 600 km s^{-1} to account for the difference between the optical depths of the observed feature and the photosphere (see text). The model IDs are shown in the legends.

N. N. Chugai 2024 for an example). None of the models considered here, however, fall into this category based on the velocity curve alone.

4.2.1. Comparison with STELLA Models

In order to make more quantitative statements about the similarity between the observed luminosity/velocity curves and those from the models, first, we measured the key observable parameters of the SNEC LCs in order to compare them with the actual observed ones. Here the following parameters are considered, adopting the definitions by J. A. Goldberg et al. 2019): the length of the plateau (t_p) in days; the luminosity at day +50 (L_{50}) in 10^{42} erg s^{-1} and the velocity at the photosphere at day +50 (v_{50}) in km s^{-1}. These parameters, inferred from the SNEC models, are collected in Table 3 and plotted in Figure 6. In the last row we show the actually observed values for SN 2023ixf (plotted with an asterisk), where the measured velocity has been corrected by -600 km s^{-1} as explained above.

Second, we applied the analytical formulae of J. A. Goldberg et al. (2019) to estimate the observable parameters from STELLA (S. I. Blinnikov et al. 1998) models. The following parameters, taken from the input progenitor models for SNEC, are used in these calculations: the radius of the progenitor in 500 $R_\odot$ units (R_{500}), the ejecta mass in 10 $M_\odot$ units (M_{10}), the nickel mass in $M_\odot$ ($M_{\rm Ni}$), and the final energy of the explosion in 10^{51} erg (E_{51}). We considered E_{51} as a free parameter within the range of $1 < E_{51} < 2$ covered by our SNEC models, and estimated t_p, L_{50} and $v_{\rm Fe} \approx v_{\rm phot} + 600$ km s^{-1} using the equations given by J. A. Goldberg et al. (2019). The results are plotted together with the SNEC observables in Figure 7.

Table 3
Observable Parameters Inferred from SNEC Models (see text)

Model	t_p (days)	L_{50} (10^{42} erg s^{-1})	v_{50} (km s^{-1})
M11	81	1.50	3298
M11-csm1	74	2.06	3752
M11-csm2	73	2.27	3927
M11-csm3	72	2.16	3752
M11-csm4	72	2.02	3637
M11-csm5	73	2.42	3952
M12	62	2.40	3973
M12-csm	63	2.66	4249
M12-2-csm	71	2.27	4023
M15o	85	3.26	4336
M15o-csm1	87	3.32	4345
M15o-csm2	86	3.74	4771
M15o-ni	84	3.45	4369
M15n	66	2.15	3701
M15n-csm	66	2.75	4124
M15n0-csm	70	2.37	3894
M15n1-csm	70	2.42	3922
M15n2-csm	67	2.69	4115
M20	77	3.43	4492
M20-csm	79	3.58	4612
M20-2-csm	89	2.66	4023
M20-3-csm	82	3.12	4345
M20-csm2	79	4.20	4989
M25	87	2.66	4134
M25-csm	87	2.80	4299
SN 2023ixf	81	1.96	3750

Note. The last row gives the actually observed values from the bolometric LC and velocity curve of SN 2023ixf.

From Figure 6 it is seen that the observable parameters inferred from our SNEC models suggest the same conclusion as the visual inspection of the LCs and the velocities did in the previous section: the parameters of SN 2023ixf are most similar to the observables of the M11 models, even though no model gives a perfect match. The high-mass models (M15o, M20, and M25) predict too high L_{50} and v_{50} values. The M15n models have similar L_{50} than the M11 and M12 models, but their t_p values are too low compared to the observed plateau length. It is also clear from the velocity–luminosity relation (bottom panel in Figure 6) that SN 2023ixf is most consistent with the predictions of the low-mass SNEC models.

Very similar conclusion can be drawn from the comparison with STELLA models in Figure 7. Even though STELLA generally predicts longer plateau phases than SNEC (as shown in the middle panel), it is seen that the observed parameters of SN 2023ixf, indicated by the horizontal dashed line in each panel, are closer to the red curves that correspond to the progenitor parameters of the M11 models. The agreement is best within the range of $1.2 < E_{51} < 1.6$, which is also consistent with the results from SNEC models.

It is concluded that the comparison of the observable parameters predicted by both SNEC and STELLA hydrodynamical models suggests that SN 2023ixf had a relatively low-mass ejecta, $M_{\rm ej} < 9\ M_\odot$ after the core collapse of an $M \sim 10$–$11\ M_\odot$ progenitor. Our result is consistent with the conclusions of M. C. Bersten et al. (2024), who also found that the best-fitting hydrodynamical model contains a relatively low-mass $M_{\rm ej} \sim 10\ M_\odot$ ejecta. Despite this agreement, however, as it is seen in Figure 5, none of the hydrodynamical models presented in this paper can reproduce the entire bolometric LC adequately.

4.3. Effects of Different CSM Parameters on the Bolometric LC

SN 2023ixf was embedded in a dense, confined CSM that significantly affected the early LC as well as the spectral evolution during the first 10–15 days after explosion, which was extensively modeled in previous studies (G. Li et al. 2024; L. Martinez et al. 2024; E. A. Zimmerman et al. 2024; A. Kozyreva et al. 2025). We attempted to investigate whether adding such a CSM on top of the progenitor model in SNEC had an overall impact on estimating the ejecta physical parameters from LC modeling. Details on the attached CSM are given in Section 3.2. Following V. Morozova et al. (2016), the mass and outer radius of the attached CSM ($M_{\rm csm}$ and $R_{\rm csm}$, respectively) were varied in between 0.35 and 0.50 $M_\odot$ and 20–60 $\times$ 10^{13} cm, respectively (see Table 2). The choice of these parameter ranges were motivated by the results of our semianalytic modeling, namely the parameters of the "shell" component, given in Table 1. The density profiles of the attached CSM models are shown in the top panel of Figure 8.

The final LCs of the M11 model family (see Table 2) are plotted in the bottom panel of Figure 8, together with the observations. It is apparent that the early peaks of the model LCs are too high, by a factor of ∼100, compared to the observations. A similar result was presented recently by A. Kozyreva et al. (2025). Note that the sharp first peak of the SNEC model LCs corresponds to very high temperatures shortly after the shock breakout. This peak is visible on the very short-cadence bolometric LC published by L. Martinez et al. (2024), but missing from our estimated bolometric luminosity curve of SN 2023ixf. Nevertheless, the detailed CSM modeling by L. Martinez et al. (2024) reproduced the first luminosity peak of SN 2023ixf, reaching $L_{\rm bol} \sim 10^{45}$ erg s^{-1}, which is similar to peak of our ejecta+CSM model LCs plotted in Figure 8. On the other hand, even if we disregard the first sharp peak, all SNEC model LCs that contain CSM are still too bright during the first ∼20 days after explosion. All the other models containing CSM show similar behavior (see Figure 5). Thus, it seems that the assumed mass and radius of the CSM, similar to those of the "shell" component in Table 1, gives a CSM that is too dense to be compatible with the observed LC.

On the other hand, Figure 8 also shows that after ∼30 days the LCs containing the CSM contribution start to become similar to the LC without the CSM, in agreement with the calculations presented by V. Morozova et al. (2016). Thus, instead of optimizing the CSM parameters to better fit the early part of the LC, we focus on the later part of the plateau, after ∼30 days, when the contribution from the confined CSM becomes weak. This is also the phase when the first P Cygni features of H and He started to appear in the optical spectrum (e.g., R. S. Teja et al. 2023; K. A. Bostroem et al. 2024), suggesting the emergence of the SN ejecta from behind the CSM.

These calculations suggest that the ejecta mass estimate based on the bolometric LC after ∼30 days is not sensitive to the presence or absence of a dense, confined CSM, since the

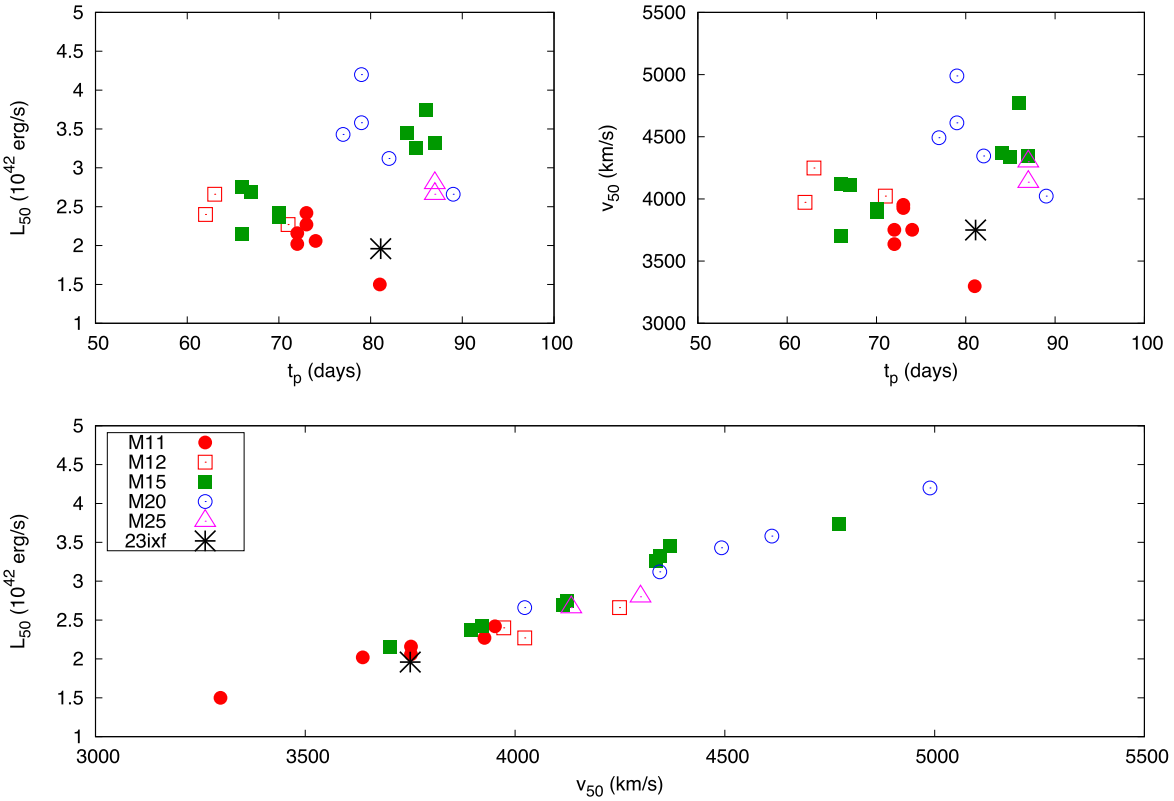

Figure 6. The observable parameters from SNEC models (see Table 3) compared with the observed values of SN 2023ixf (asterisk).

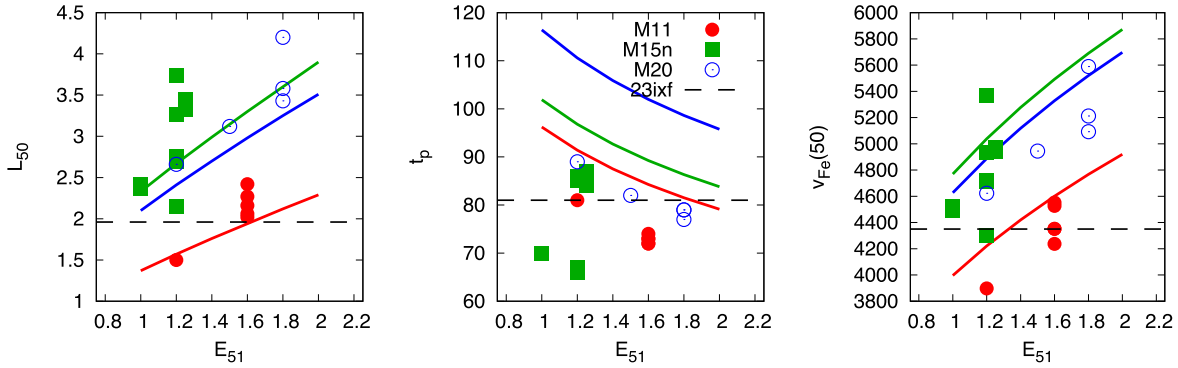

Figure 7. Comparison of the observables from SNEC (symbols) and from STELLA (curves) against the kinetic energy E_{51}. The dashed lines indicate the observed values for SN 2023ixf.

CSM contribution on the LC becomes weak after this phase. Therefore, our conclusion that the M11-csm1 model gives the most similar LC to the observations of SN 2023ixf (Sections 4.2 and 4.2.1) becomes unaffected.

4.4. Effects of Extended ^{56}Ni Distribution on the Bolometric LC

Even though the length of the LC plateau (t_p) is found to be a useful indicator for the ejecta mass (e.g., I. Y. Litvinova & D. K. Nadezhin 1985; D. K. Nadyozhin 2003; A. P. Nagy et al. 2014), the relation between them is not unique: Δt_P also depends on the explosion energy, the progenitor radius, and other parameters as well (see, e.g., A. P. Nagy et al. 2014; J. A. Goldberg et al. 2019; V. P. Utrobin et al. 2021). Recently, a particularly interesting case was explored by V. P. Utrobin & N. N. Chugai (2024): from hydrodynamical modeling they found that the short plateau length of SN 2018gj ($t_p \sim 75$ days) can be explained by a relatively massive ejecta, $M_{\rm ej} \gtrsim 20\,M_\odot$, and an asymmetric distribution of ^{56}Ni extending to high velocities ($v_{\rm Ni}^{\rm max} \gtrsim 5000$ km s^{-1}). Similar bipolar Ni-distribution was found also in SN 2017gmr (V. P. Utrobin et al. 2021). In such a bipolar Ni-distribution some of the γ-rays released by the radioactive decay closer to the photosphere may escape more easily than the photons created deeper within the ejecta. Thus, γ-ray leaking becomes stronger, even during the plateau phase, resulting in less efficient heating of the ejecta, which enhances hydrogen recombination and reduces the plateau length.

Since the plateau length was one of the observables that was used to constrain the ejecta mass of SN 2023ixf in Sections 4.1

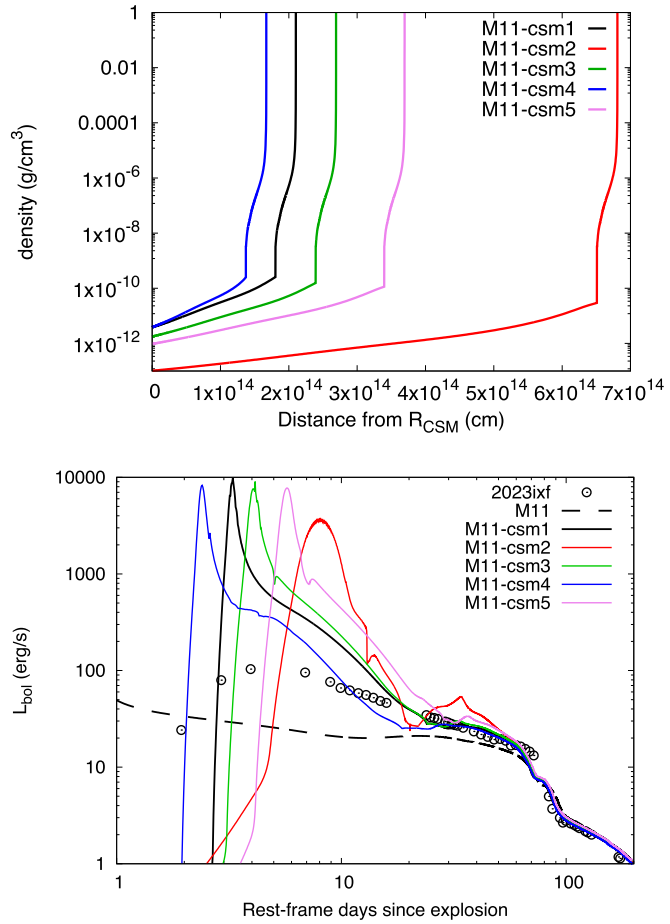

Figure 8. Top panel: the density distribution of the various M11-csm models listed in Table 2. Note that the distance from the outmost surface of the CSM envelope (in cm) is plotted on the horizontal axis due to the convention used by SNEC. The innermost part of the SN envelope is omitted for display purposes. Bottom panel: the luminosity evolution of the various M11-csm models (colored curves) compared with the observations (red symbols). The LC from the M11 model without the CSM (dotted curve) is also shown for comparison.

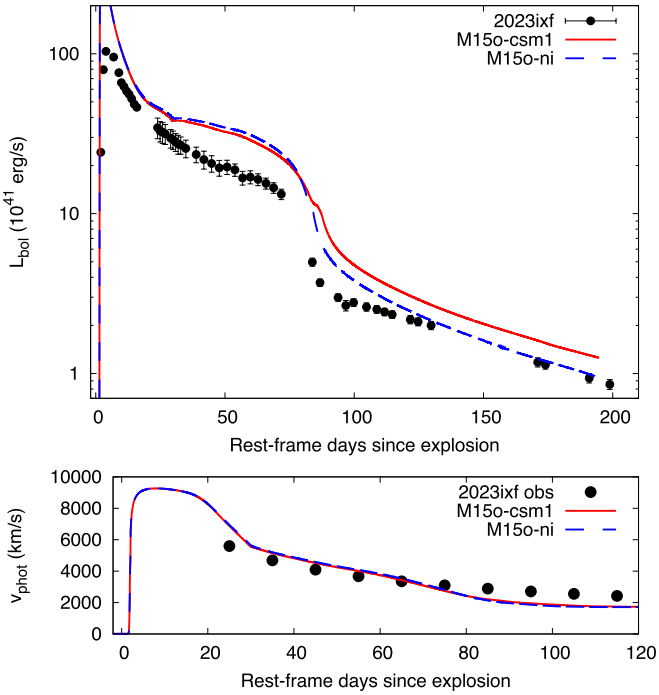

Figure 9. The effect of the extended Ni-distribution (model M15o-ni, plotted with blue dashed line) on the light curve (top panel), and on the velocity curve (bottom panel) compared with the observations (black circles) and the M15o-csm1 model (red lines).

and 4.2, we attempted to address this issue with SNEC, even though the applicability of this 1D-hydrocode for modeling this problem is very limited. Nevertheless, we computed a variant of the M15o-csm1 model (see Table 2) with the outer mass coordinate of the Ni-distribution extending up to 12 $M_\odot$, i.e., close to the surface of exploding star (model M15o-ni). The resulting LC is plotted in Figure 9 together with the observations and the original M15o-csm1 LC.

It is seen that even within this simple model the extended Ni-distribution reduces the length of the plateau as well as the LC level during the early tail phase, but its effect is not strong enough: the shortening of t_p is only a few days compared to the plateau length of the original model having centrally located ^{56}Ni. Thus, the resulting LC is still less compatible with the observations of SN 2023ixf than the LCs produced by the models having less massive ejecta. It is concluded that while the Ni-distribution can certainly affect the fundamental properties of the model LCs, this effect is less pronounced in SNEC models, probably due to its simplified 1D (spherical) geometry. A more comprehensive study of this problem, which requires at least 2D modeling, is beyond the scope of the present paper.

5. Conclusions

By modeling the bolometric LC constructed from observations, we confirm the relatively low-mass ejecta of SN 2023ixf ($M_{ej} \sim$ 8–9 $M_\odot$), consistent with the results of D. Hiramatsu et al. (2023), M. C. Bersten et al. (2024), A. Singh et al. (2024), B. Hsu et al. (2025), and S. Forde & J. A. Goldberg (2025).

Applying the semianalytic LC2 code we get ∼7.8 $M_\odot$ for the ejecta (core + shell) mass, with an uncertainty range of ∼1 $M_\odot$, which, together with the other physical parameters listed in Table 1, is able to explain both the plateau length as well as the late-phase decline rate self-consistently. A comparison with SN 2017eaw, which showed both a longer plateau and a shallower late-phase decline, revealed that SN 2013ixf had a factor of ∼2 less massive ejecta than SN 2017eaw. Taking into account the mass of the neutron star (∼1.5 $M_\odot$) as well as some mass-loss during the evolution after the main sequence, these results are consistent with a progenitor mass of $M_{prog} \sim 10\,M_\odot$ and $\sim 17\,M_\odot$ for SN 2023ixf, and SN 2017eaw, respectively.

The synthesized LCs from SNEC simulations of massive stars fully support these results (see Table 2). Even though the SNEC LCs do not extend to sufficiently late phases, the luminosity and the length of the plateau of the simulated LC constrains the ejecta mass. From these SNEC models the most likely ejecta mass, ∼9 $M_\odot$, is somewhat higher but similar to the value provided by the LC2 code. Our results are consistent with those from M. C. Bersten et al. (2024) regarding the ejecta parameters. However, none of the SNEC hydrodynamical models presented in this paper can adequately fit the entire bolometric LC of SN 2023ixf, especially during the first month when the ejecta–CSM interaction had the strongest effect.

Acknowledgments

The operation of the RC 80 and BRC80 telescopes were supported by the GINOP 2.3.2-15-2016-00033 project of the National Research, Development and Innovation Office (NKFIH), Hungary, based on funding from the European Union. This research was supported by NKFIH OTKA grants K-142534, K-138962, FK-134432, and NKFIH KKP-143986 grant. L.K. acknowledges the support of the NKFIH grant PD-134784. K.V. is supported by the Bolyai János Research Scholarship of the Hungarian Academy of Sciences. A.B., C. K. and A.S. were supported by the "SeismoLab" KKP-137523 Élvonal grant of the NKFIH. Zs.B. was supported by the ÚNKP-22-2 New National Excellence Program of the Hungarian Ministry for Culture and Innovation from the source of the NKFIH Fund. N.O.SZ. thanks the financial support provided by the undergraduate research assistant program of Konkoly Observatory.

Software: LC2 (A. P. Nagy & J. Vinkó 2016); SNEC (V. Morozova et al. 2015).

ORCID iDs

József Vinkó https://orcid.org/0000-0001-8764-7832
Zsófia Réka Bodola https://orcid.org/0009-0006-4162-5447
Ákos Gődény https://orcid.org/0009-0001-3178-603X
Szelina Fruzsina Csák https://orcid.org/0009-0000-0914-130X
Réka Könyves-Tóth https://orcid.org/0000-0002-8770-6764
Andrea P. Nagy https://orcid.org/0000-0002-9324-3903
Tamás Szalai https://orcid.org/0000-0003-4610-1117
Dominik Bánhidi https://orcid.org/0009-0000-9929-7518
Imre Barna Bíró https://orcid.org/0000-0001-9061-2147
Attila Bódi https://orcid.org/0000-0002-8585-4544
Zsófia Bora https://orcid.org/0000-0001-6232-9352
Borbála Cseh https://orcid.org/0000-0002-6497-8863
Tibor Hegedüs https://orcid.org/0009-0004-3558-8948
Ágoston Horti-Dávid https://orcid.org/0009-0008-2052-8474
András Péter Joó https://orcid.org/0000-0001-5203-434X
Csilla Kalup https://orcid.org/0000-0002-1663-0707
Levente Kriskovics https://orcid.org/0000-0002-1792-546X
András Pál https://orcid.org/0000-0001-5449-2467
Zsolt Regály https://orcid.org/0000-0001-5573-8190
Bálint Seli https://orcid.org/0000-0002-3658-2175
Ádám Sódor https://orcid.org/0000-0001-7806-2883
Norton Olivér Szabó https://orcid.org/0009-0007-1015-0327
Róbert Szakáts https://orcid.org/0000-0002-1698-605X
Krisztián Vida https://orcid.org/0000-0002-6471-8607

References

Arnett, W. D. 1980, ApJ, 237, 541
Arnett, W. D. 1982, ApJ, 253, 785
Arnett, W. D., & Fu, A. 1989, ApJ, 340, 396
Barker, B. L., Harris, C. E., Warren, M. L., O'Connor, E. P., & Couch, S. M. 2022, ApJ, 934, 67
Barna, B., Nagy, A. P., Bora, Z., et al. 2023, A&A, 677, A183
Bersten, M. C., Orellana, M., Folatelli, G., et al. 2024, A&A, 681, L18
Blinnikov, S. I., Eastman, R., Bartunov, O. S., Popolitov, V. A., & Woosley, S. E. 1998, ApJ, 496, 454
Bostroem, K. A., Sand, D. J., Dessart, L., et al. 2024, ApJL, 973, L47
Branch, D., & Wheeler, J. C. 2017, Supernova Explosions (Berlin: Springer)
Colgate, S. A., Petschek, A. G., & Kriese, J. T. 1980, ApJL, 237, L81
Cosentino, S. P., Pumo, M. L., & Cherubini, S. 2025, MNRAS, 540, 2894
Dickinson, D., Milisavljevic, D., Garretson, B., et al. 2025, ApJ, 984, 71
Fang, Q., Moriya, T. J., Ferrari, L., et al. 2025, ApJ, 978, 36
Ferrari, L., Folatelli, G., Ertini, K., Kuncarayakti, H., & Andrews, J. 2024, A&A, 687, L20
Folatelli, G., Ferrari, L., Ertini, K., Kuncarayakti, H., & Maeda, K. 2025, A&A, 698, A213
Forde, S., & Goldberg, J. A. 2025, RNAAS, 9, 135
Glebbeek, E., Gaburov, E., de Mink, S. E., Pols, O. R., & Portegies Zwart, S. F. 2009, A&A, 497, 255
Goldberg, J. A., Bildsten, L., & Paxton, B. 2019, ApJ, 879, 3
Hiramatsu, D., Tsuna, D., Berger, E., et al. 2023, ApJL, 955, L8
Hsu, B., Smith, N., Goldberg, J. A., et al. 2025, ApJ, 990, 148
Itagaki, K. 2023, TNSTR 178084, Transient Name Server
Jacobson-Galán, W. V. 2025, Univ, 11, 231
Jencson, J. E., Pearson, J., Beasor, E. R., et al. 2023, ApJL, 952, L30
Jermyn, A. S., Bauer, E. B., Schwab, J., et al. 2023, ApJS, 265, 15
Kasen, D., & Bildsten, L. 2010, ApJ, 717, 245
Kilpatrick, C. D., Foley, R. J., Jacobson-Galán, W. V., et al. 2023, ApJL, 952, L23
Kozyreva, A., Caputo, A., Baklanov, P., Mironov, A., & Janka, H.-T. 2025, A&A, 694, A319
Kumar, A., Dastidar, R., Maund, J. R., Singleton, A. J., & Sun, N.-C. 2025, MNRAS, 538, 659
Kuriyama, N., & Shigeyama, T. 2020, A&A, 635, A127
Li, G., Hu, M., Li, W., et al. 2024, Natur, 627, 754
Li, G., Wang, X., Yang, Y., et al. 2025, arXiv:2504.03856
Litvinova, I. Y., & Nadezhin, D. K. 1985, SvAL, 11, 145
Liu, C., Chen, X., Er, X., et al. 2023, ApJL, 958, L37
Martinez, L., Bersten, M. C., Folatelli, G., Orellana, M., & Ertini, K. 2024, A&A, 683, A154
Michel, P. D., Mazzali, P. A., Perley, D. A., Hinds, K. R., & Wise, J. L. 2025, MNRAS, 539, 633
Moriya, T. J., & Singh, A. 2024, PASJ, 76, 1050
Morozova, V., Piro, A. L., Renzo, M., & Ott, C. D. 2016, ApJ, 829, 109
Morozova, V., Piro, A. L., Renzo, M., et al. 2015, ApJ, 814, 63
Morozova, V., & Stone, J. M. 2018, ApJ, 867, 4
Nadyozhin, D. K. 2003, MNRAS, 346, 97
Nagy, A. P., Ordasi, A., Vinkó, J., & Wheeler, J. C. 2014, A&A, 571, A77
Nagy, A. P., & Vinkó, J. 2016, A&A, 589, A53
Neustadt, J. M. M., Kochanek, C. S., & Smith, M. R. 2024, MNRAS, 527, 5366
Niu, Z., Sun, N.-C., Maund, J. R., et al. 2023, ApJL, 955, L15
Nugis, T., & Lamers, H. J. G. L. M. 2000, A&A, 360, 227
Paxton, B., Bildsten, L., Dotter, A., et al. 2011, ApJS, 192, 3
Paxton, B., Cantiello, M., Arras, P., et al. 2013, ApJS, 208, 4
Paxton, B., Marchant, P., Schwab, J., et al. 2015, ApJS, 220, 15
Paxton, B., Schwab, J., Bauer, E. B., et al. 2018, ApJS, 234, 34
Paxton, B., Smolec, R., Schwab, J., et al. 2019, ApJS, 243, 10
Pledger, J. L., & Shara, M. M. 2023, ApJL, 953, L14
Qin, Y.-J., Zhang, K., Bloom, J., et al. 2024, MNRAS, 534, 271
Ransome, C. L., Villar, V. A., Tartaglia, A., et al. 2024, ApJ, 965, 93
Riess, A. G., Yuan, W., Macri, L. M., et al. 2022, ApJL, 934, L7
Shrestha, M., DeSoto, S., Sand, D. J., et al. 2025, ApJL, 982, L32
Singh, A., Teja, R. S., Moriya, T. J., et al. 2024, ApJ, 975, 132
Soraisam, M., Matheson, T., Andrews, J., et al. 2023, ATel, 16050, 1
Szalai, T., Vinkó, J., Könyves-Tóth, R., et al. 2019, ApJ, 876, 19
Teja, R. S., Singh, A., Basu, J., et al. 2023, ApJL, 954, L12
Tsuna, D., & Takei, Y. 2023, PASJ, 75, L19
Tsuna, D., Takei, Y., Kuriyama, N., & Shigeyama, T. 2021, PASJ, 73, 1128
Utrobin, V. P., & Chugai, N. N. 2024, Ap&SS, 369, 49
Utrobin, V. P., Chugai, N. N., Andrews, J. E., et al. 2021, MNRAS, 505, 116
Valenti, S., Benetti, S., Cappellaro, E., et al. 2008, MNRAS, 383, 1485
Van Dyk, S. D., Srinivasan, S., Andrews, J. E., et al. 2024, ApJ, 968, 27
Xiang, D., Mo, J., Wang, L., et al. 2024, SCPMA, 67, 219514
Yang, Y.-P., Liu, X., Pan, Y., et al. 2024, ApJ, 969, 126
Zheng, W., Dessart, L., Filippenko, A. V., et al. 2025, ApJ, 988, 61
Zimmerman, E. A., Irani, I., Chen, P., et al. 2024, Natur, 627, 759